PNAS RESEARCH ARTICLE | EARTH, ATMOSPHERIC, AND PLANETARY SCIENCES

High-resolution geostationary satellite observations of free tropospheric NO_2 over North America and implications for lightning emissions

Ruijun Dang[a,1], Daniel J. Jacob[a], Huiqun Wang[b], Caroline R. Nowlan[b], Gonzalo Gonzalez Abad[b], Heesung Chong[b], Xiong Liu[b], Viral Shah[c,d], Laura H. Yang[a], Yujin J. Oak[a], Eloise A. Marais[e], Rebekah P. Horner[e], Andrew W. Rollins[f], James H. Crawford[g], Ke Li[h], and Hong Liao[h]

Affiliations are included on p. 6.

Edited by Thomas Wagner, Max-Planck Institut for Chemie, Mainz, Germany; received April 28, 2025; accepted September 10, 2025 by Editorial Board Member Akkihebbal R. Ravishankara

Free tropospheric (FT) nitrogen dioxide (NO_2) plays a critical role in atmospheric oxidant chemistry as a source of tropospheric ozone and of the hydroxyl radical (OH). It also contributes significantly to satellite-observed tropospheric NO_2 columns, which should be considered when using these columns to quantify surface emissions of nitrogen oxide radicals ($NO_x \equiv NO + NO_2$). But large uncertainties remain in the sources and chemistry of FT NO_2 because observations are sparse. Here, we construct a cloud-sliced FT NO_2 (700 to 300 hPa) product from the Tropospheric Emissions: Monitoring of Pollution (TEMPO) geostationary satellite instrument over North America. This product provides higher data density and quality than previous products from low Earth orbit instruments, including the first observations of the FT NO_2 diurnal cycle in different seasons. Combined with coincident observations from the Geostationary Lightning Mapper, the TEMPO data imply that lightning is the dominant source of FT NO_x in nonwinter seasons. Comparison of TEMPO FT NO_2 data with the Goddard Earth Observation System-Composition Forecasts (GEOS-CF) atmospheric chemistry model shows overall consistent magnitudes, seasonality, and diurnal variation, with a midday minimum in nonwinter seasons from photochemical loss. However, there are major discrepancies that we attribute to GEOS-CF's use of a standard cloud-top-height-based scheme for the lightning NO_x source. We find that this scheme underestimates offshore lighting flash density and misrepresents the diurnal cycle of lightning over land. Our FT NO_2 product provides a unique resource for improving the lightning NO_x parameterization in atmospheric models and the ability to use NO_2 observations from space to quantify surface NO_x emissions.

nitrogen dioxide | free troposphere | geostationary satellites | diurnal cycle | lightning

Significance

Free tropospheric (FT) nitrogen dioxide (NO_2) drives global atmospheric oxidant chemistry, but its observations are sparse and its sources and chemistry are uncertain. Applying cloud-slicing to the Tropospheric Emissions: Monitoring of Pollution (TEMPO) geostationary satellite instrument, we produce a unique high-quality FT NO_2 dataset over North America including the first measurements of the diurnal cycle. Comparison with coincident geostationary lightning observations suggests that lightning dominates the FT NO_2 source in nonwinter seasons over North America and that a commonly used parameterization of this source in atmospheric chemistry models has large errors. Correcting these errors is essential for models to properly describe global oxidant chemistry.

The free troposphere (FT), extending from the top of the planetary boundary layer (PBL) at about 2 km altitude up to the tropopause, contains most of total atmospheric mass. It largely determines the abundance of tropospheric ozone and of the hydroxyl radical (OH), the main atmospheric oxidant, through chemistry catalyzed by nitrogen oxide radicals ($NO_x \equiv NO + NO_2$) (1–4). While the PBL is in daily contact with surface sources of NO_x through the diurnal cycle of surface heating and vertical mixing, the FT is more isolated from the surface. Sources of FT NO_x include lightning, aviation, lofted fire plumes, frontal and deep convective lifting of surface NO_x originating from fuel combustion and soils, and stratospheric downwelling. Lightning is thought to dominate the supply of FT NO_x except in winter (5–7). However, there are large uncertainties in the magnitude and distribution of this lightning source (8–13). FT NO_x chemistry is also not well understood, complicated by aerosol processes and organic nitrate reservoirs (6, 14–16). Addressing these uncertainties is critical for understanding tropospheric oxidant chemistry.

Progress in understanding NO_x sources and chemistry in the FT has been limited by the sparsity of observations. In situ measurements are only available from aircraft with limited spatial and temporal coverage. Cloud slicing of NO_2 columns measured from satellites can provide more extensive coverage. It involves retrieving NO_2 columns over adjacent fully cloudy scenes with different cloud pressures. The retrieved NO_2 column is mainly restricted to the atmosphere above cloud top, so that a regression of NO_2 columns versus cloud pressure gives a measure of FT NO_2 mixing ratio (17). Several studies have applied this cloud-slicing method to infer FT NO_2 from low Earth orbit (LEO) satellite instruments, including Ozone Monitoring Instrument (OMI) (17–19) and more recently TROPOspheric Monitoring Instrument (TROPOMI) (11, 20). However, the sparse sampling from LEO limits the ability to collect adjacent fully cloudy scenes. Marais et al. (19) found that OMI-based cloud-sliced FT NO_2

The authors declare no competing interest.

This article is a PNAS Direct Submission. T.W. is a guest editor invited by the Editorial Board.

[1]To whom correspondence may be addressed. Email: rjdang@g.harvard.edu.

This article contains supporting information online at https://www.pnas.org/lookup/suppl/doi:10.1073/pnas.2510535122/-/DCSupplemental.

Published October 14, 2025.

products required averaging over thousands of kilometers to achieve significant correlations with aircraft NO_2 observations. Horner et al. (11) developed a seasonal 1° × 1° resolution product from TROPOMI, but its evaluation against aircraft observations was limited to broad regional averages.

Here, we show that NO_2 column observations from the new Tropospheric Emissions: Monitoring of Pollution (TEMPO) geostationary satellite instrument launched in April 2023 provide an unprecedented capability to measure FT NO_2 by cloud slicing with high observation density and accuracy. TEMPO is the first geostationary satellite instrument to monitor atmospheric composition over North America (21). It provides unique hourly daytime NO_2 and cloud observations with finer spatial resolution (2.0 × 4.75 km^2 at 33.5°N) than LEO instruments, enabling a first observation of the diurnal cycle of FT NO_2 to test our understanding of NO_x sources and chemistry. Combining the TEMPO cloud-sliced FT NO_2 observations with concurrent lightning observations from the Geostationary Lightning Mapper (GLM) (22) enables evaluation of the lightning NO_x source parameterizations in current atmospheric chemistry models. Aside from its intrinsic interest, an accurate cloud-sliced FT NO_2 product is also critical for using the satellite measurements of NO_2 columns to infer surface NO_x emissions in North America, because the FT makes an important and sometimes dominant contribution to the tropospheric NO_2 column that needs to be separated from the PBL (23–26).

Results and Discussion

Free Tropospheric (FT) NO_2 Observations from TEMPO. We define the FT as the 700 to 300 hPa pressure range and derive FT NO_2 mixing ratios on a 0.5° × 0.625° (~50 × 50 km^2) grid from the regression slope of above-cloud NO_2 columns versus cloud pressures for TEMPO fully cloudy pixels. *SI Appendix*, Fig. S1 illustrates this FT NO_2 derivation for a 50 × 50 km^2 domain sampled by TEMPO over Boston (December 18, 2023, at 11:15 am), illustrating the high density of available information. We perform such retrievals for all suitably cloudy scenes in the full-year TEMPO record from 1 October 2023 to 30 September 2024 and aggregate the results to produce a seasonal 2° × 2.5° product (*Materials and Methods*).

The Fig. 1, *Left* column shows the spatial distribution and seasonal mean variability of FT NO_2 over North America observed by TEMPO. The average FT NO_2 varies from 13 pptv in winter to 24 pptv in spring–summer, in contrast to surface NO_2 which peaks in winter when the NO_x lifetime is longest (27). The spring–summer maximum in FT NO_2 aligns with the seasonal peak in lightning activity, suggesting a dominant lightning contribution during these seasons, consistent with previous model studies (6, 28, 29). This attribution is further supported by spatial correlations between FT NO_2 and GLM lightning observations from the NOAA Geostationary Operational Environmental Satellites (GOES; *Materials and Methods*) in nonwinter seasons (r = 0.35 to 0.53; *SI Appendix*, Fig. S2). FT NO_2 also shows a smoother spatial variability than surface NO_2, which we attribute to a longer lifetime and chemical recycling. This smoother spatial variability is also seen in aircraft observations (23). The highest FT NO_2 concentrations are found over regions with frequent lightning (eastern US during spring-summer), strong surface pollution uplift (Mexico City year-round), and intense fire events (southern Mexico in spring; *SI Appendix*, Fig. S3). Wintertime data in Fig. 1 are limited due to fewer high-reaching clouds. In high-altitude regions like Mexico City, the PBL can occasionally extend above 700 hPa (especially in

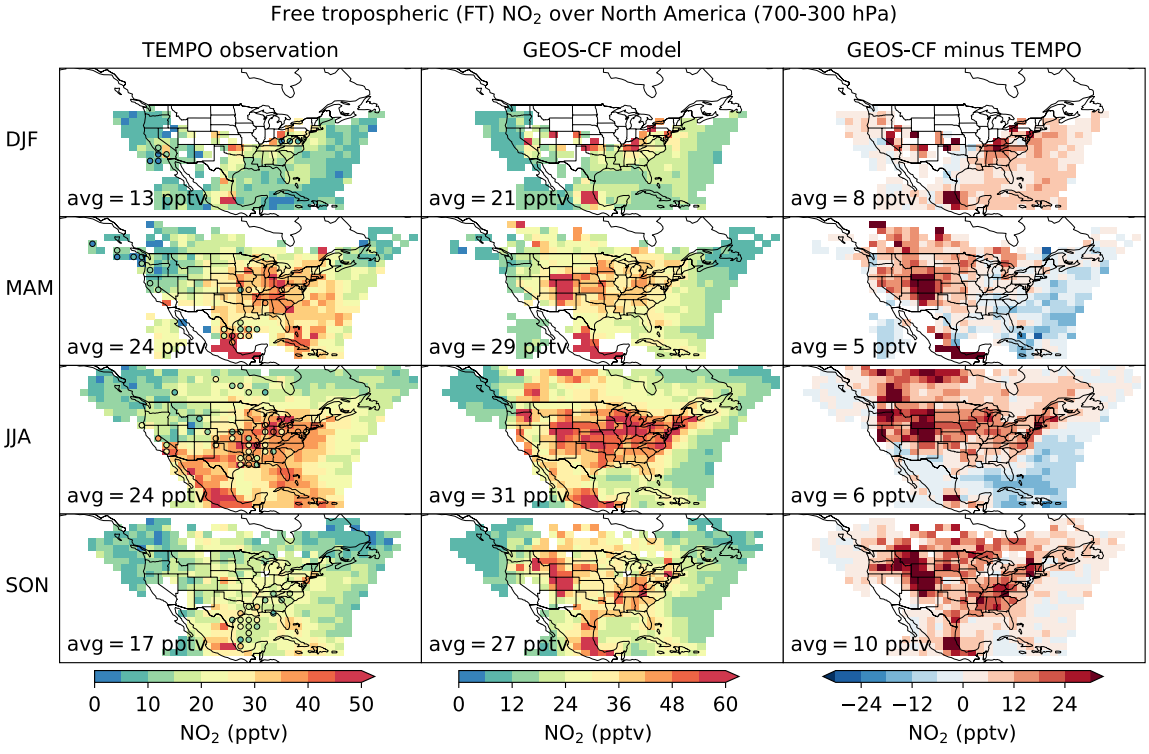

Fig. 1. FT (700 to 300 hPa) NO_2 mixing ratio over North America for different seasons of October 2023–September 2024. TEMPO observations are seasonally averaged on a 2° × 2.5° grid using all retrievals in its daytime observing window (8 to 15 LT for winter; 7 to 16 LT for spring and fall; 6 to 17 LT for summer). The product is compared to observations from a collection of aircraft campaigns in different years (circles) and to model results from Goddard Earth Observation System—Composition Forecasts (GEOS-CF) sampled at the same locations and times. The difference between the two is shown in the third column. White areas are either outside the TEMPO field of regard (FOR) or do not have sufficient full-cloud scenes for application of the cloud-sliced method. Spatial average values for the observation domains are shown *Inset*. The aircraft campaigns are listed in *SI Appendix*, Table S1 and further evaluation of the TEMPO product with these observations is in Fig. 2.

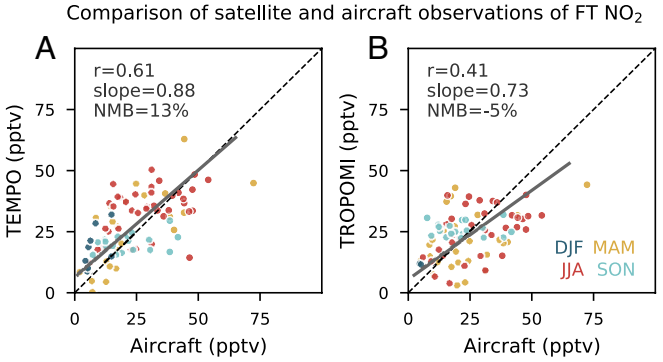

Fig. 2. Comparison of cloud-sliced FT NO_2 with aircraft observations over North America. (*A*) TEMPO product as described in Fig. 1. (*B*) TROPOMI product from Horner et al. (11) for June 2018–May 2022, processed at the same pressure range and spatial resolution as TEMPO. Aircraft observations are from the collection of INTEX-B, ARCTAS, DC-3, SEAC^{4}RS, DISCOVER-AQ, FRAPPE, WINTER, and AEROMMA campaigns, averaged seasonally on a 2° × 2.5° grid. Both TEMPO and aircraft observations are averages over the daytime window, while TROPOMI product is for the overpass time of 13:30 LT. Comparison statistics include the correlation coefficient (r), reduced major axis (RMA) regression line and slope, and NMB. The 1:1 line is shown as dashed.

summer), causing the cloud-sliced product to include some PBL influence and thus not fully represent FT conditions.

The FT NO_2 derived from cloud-slicing is representative of cloudy conditions. To assess the difference with all-sky conditions, we used model output from the NASA Goddard Earth Observation System—Composition Forecast (GEOS-CF) v1, which provides the NO_2 vertical shape factors for TEMPO retrievals. GEOS-CF FT NO_2 sampled at TEMPO cloud-sliced scenes is 2 to 7 pptv (11 to 24%) higher than the all-sky average depending on season, consistent with previous model results (20). This difference may reflect lightning NO_x production and frontal/convective uplift under cloudy conditions, although we show below that GEOS-CF has large errors in its representation of lightning. From the model perspective at least, the difference between cloudy and all-sky conditions is slight.

The Fig. 2*A* evaluates our seasonal TEMPO FT NO_2 product with daytime observations from aircraft campaigns averaged over the 2° × 2.5° grid. These include older campaigns conducted in 2006 to 2015 (INTEX-B, ARCTAS, DC-3, SEAC^{4}RS, DISCOVER-AQ, FRAPPE, WINTER) and the recent AEROMMA campaign in 2023 (*SI Appendix*, Table S1). The aircraft observations are of NO concentrations, with NO_2 inferred from NO/NO_2 photochemical steady state (PSS), to avoid positive artifacts from thermally unstable nitrates in the NO_2 measurement (6). We removed high-NO_2 plumes from fires, lightning, and convected pollution outflow that would be preferentially targeted by the aircraft, as identified by source tracers and flight logs (*Materials and Methods*). We find an overall good spatial/seasonal correlation between TEMPO and the aircraft observations, considering the mismatches in observing conditions and years (r = 0.61, regression slope = 0.88, NMB = 13%). The variability in the aircraft observations is largely driven by higher values in spring and summer over the eastern US, which is captured by TEMPO and attributable to lightning.

We use the difference statistics between TEMPO and aircraft observations in Fig. 2*A* to estimate an accuracy of 13% and precision of 50% for our FT NO_2 product. This precision estimate is conservative because it assumes that all of the difference between our FT NO_2 product and the aircraft observations is due to error in the FT NO_2 product. Errors and mismatch in the aircraft observations would also contribute. See *Materials and Methods* for further discussion of errors.

Our TEMPO FT NO_2 product vastly outperforms the previous LEO OMI cloud-sliced product, which exhibited poor correlation with aircraft observations at 8° × 10° resolution (17) and required continental-scale averaging to achieve satisfactory agreement (19). Horner et al. (11) more recently reported a global FT NO_2 cloud-sliced product at 1° × 1° resolution using TROPOMI, which is also in LEO but has higher spatial resolution (3.5 × 5.5 km^2) than OMI (13 × 24 km^2). They evaluated that product at broad regional scales. We show in Fig. 2*B* that it also achieves significant correlation with the aircraft observations over North America on the 2° × 2.5° grid (r = 0.41, regression slope = 0.73, NMB = −5%) though not as good as TEMPO. TROPOMI values average 20% lower than TEMPO, which we attribute in part to a 13:30 overpass local time (LT) and in part to Horner et al. (11)'s use of a geometric air mass factor (AMF) that ignores atmospheric scattering in the NO_2 retrieval (*Materials and Methods*). Comparison of spatial and seasonal variability between the TEMPO and TROPOMI products on the 2° × 2.5° grid shows a high degree of consistency (*SI Appendix*, Fig. S4 and Table S3) but TEMPO has a smoother background and better coverage in the western US and in winter, even with only 1 y of data as compared to 4 y of data for TROPOMI.

Model Errors in Lightning NO_x Emissions Revealed by TEMPO and GLM. The Fig. 1 compares TEMPO FT NO_2 observations with GEOS-CF v1 model results (30), produced by the NASA Global Modeling and Assimilation Office and distributed with the TEMPO NO_2 product for which they provide vertical shape factors in the AMF calculation. GEOS-CF uses the GEOS-Chem chemical module (emissions, chemistry, deposition) within the GEOS meteorological model and data assimilation system at 25 × 25 km^2 resolution. GEOS-CF NO_2 vertical profiles are sampled at TEMPO pixel locations and overpass times. For comparison with the TEMPO FT NO_2 product, we averaged the GEOS-CF NO_2 mixing ratio vertical profiles over the local cloud-sliced pressure ranges for the same scenes.

The comparison in Fig. 1 shows general consistency in magnitudes, spatial distributions, and seasonal variations, but there are important differences. GEOS-CF averages 5 to 10 pptv higher, mainly due to hotspots that are not present in the TEMPO observations. One group of hotspots appears over urban and/or high-altitude terrain regions, including the Rocky Mountains and Mexico City, where 700 hPa might still be within the model PBL. In addition, the GEOS-CF simulation uses the Year 2010 HTAP v2.2 inventory for anthropogenic NO_x emissions (31), which would overestimate Year 2023 emissions in the United States by a factor of 2.3 (32). Another group of hotspots is found over regions of western North America with large 2024 fires (*SI Appendix*, Fig. S3). GEOS-CF assumes that 35% of fire emissions are directly injected into the FT (3.5 to 5.5 km), which is likely excessive (33, 34). In addition, GEOS-CF and other models do not properly account for the observed rapid conversion of NO_x to organic nitrate species in fire plumes (35).

GEOS-CF overestimates FT NO_2 over land in the eastern US while underestimating FT NO_2 offshore during spring and summer, suggesting large errors in the model's parameterization of lightning emissions. This is supported by GOES GLM observations (*Materials and Methods*), as shown in Fig. 3*A*. GLM detects a high frequency of lightning flashes offshore from the eastern United States, with a spatial pattern similar to TEMPO FT NO_2. In GEOS-CF, lightning flashes are parameterized using a standard model scheme that takes cloud top height (CTH) as a proxy, with different coefficients assigned for land and ocean (Fig. 3*B*) (36). This differentiation is intended to account for higher updraft

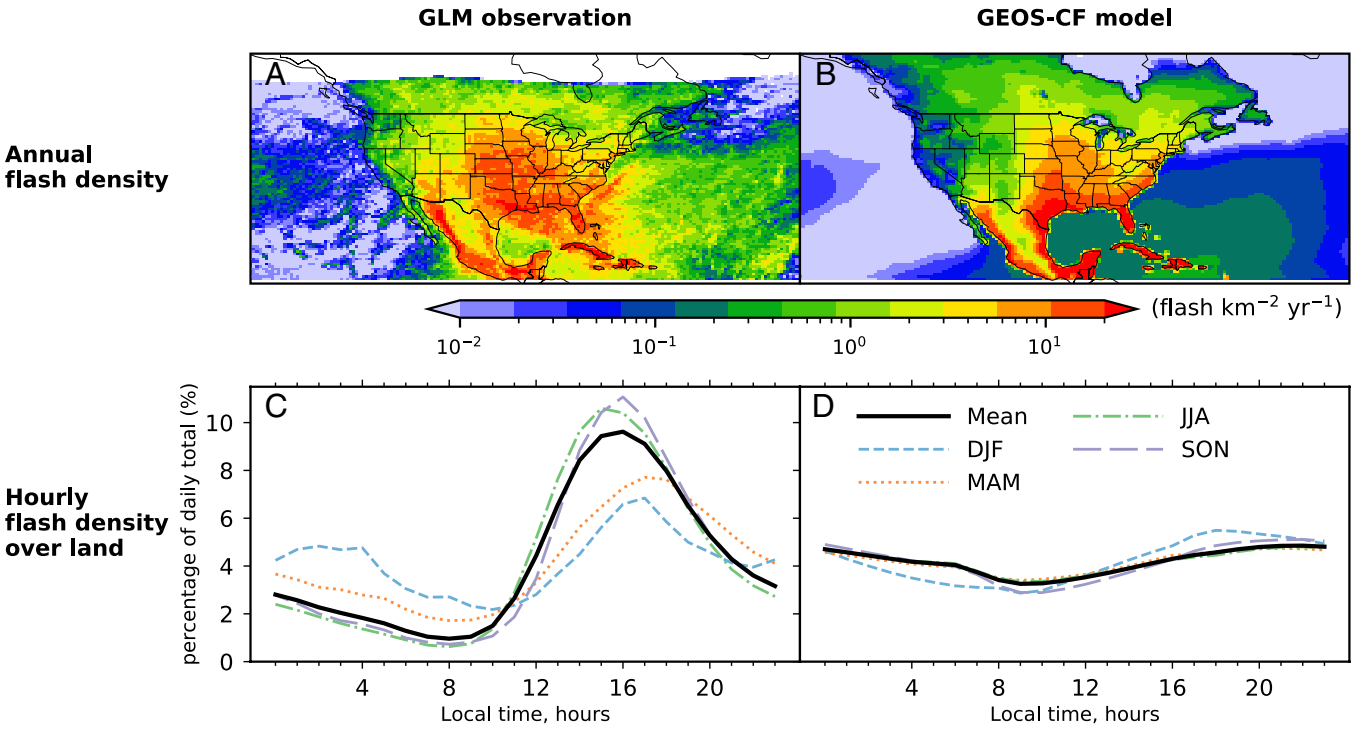

Fig. 3. Lightning flash densities over North America during October 2023 to September 2024. The *Top* panels show the annual flash density distribution (*A*) observed by the GLM and (*B*) simulated by the GEOS-CF model. The *Bottom* panels show the relative diurnal variations of seasonal and annual flash density over land from (*C*) GLM and (*D*) GEOS-CF. GLM observations are from the GOES-16 and GOES-18 Level 2 product (*Materials and Methods*). No GLM observations are available north of 54°N (in white).

velocities over land, but we find that it underestimates lightning flash frequency and resulting FT NO_2 levels over the North Atlantic. The GLM observations show a factor of 10 diurnal variation in lightning flash frequency over land from the minimum at 8 LT to the maximum at 16 LT, but GEOS-CF has little diurnal variation. GEOS-CF further applies a NO_x yield of 500 mol N flash^{-1} for regions north of 35°N, doubling the value of 260 mol N flash^{-1} used elsewhere (*SI Appendix*, Fig. S5), which likely contributes to excessive FT NO_2 over land. This adjustment was originally implemented in GEOS-Chem to match FT NO_2 observations from an older aircraft campaign (ICARTT) (37), but that dataset may have been biased high due to positive interference from nitrate reservoirs (6).

First Diurnal Observations of FT NO_2. TEMPO enables the first-ever observations of the diurnal variation of FT NO_2, as shown in Fig. 4. The data show little diurnal variation in winter and a pronounced midday minimum in other seasons. This FT NO_2 diurnal cycle differs from that previously reported from geostationary observations for the urban PBL, where the combination of emissions and chemistry drives a NO_2 increase over the course of the day in winter and a weak afternoon minimum in summer (38, 39). GEOS-CF reproduces well the diurnal variation of FT NO_2 observed by TEMPO and its seasonality, except that it exaggerates the morning decrease in summer and fall. The midday minimum outside of winter can be explained by photochemical oxidation by the OH radical and a diurnal variation in the NO/NO_2 steady-state ratio. The morning overestimate in GEOS-CF in summer–fall may be caused by excessive lightning at night and in early morning, as shown by comparison to the GLM diurnal cycle, where observed lightning during these hours is particularly low (Fig. 3 *C* and *D*). Using GLM-based diurnal lightning patterns and a lower NO_x yield per flash may improve agreement between the model and TEMPO FT NO_2. More work is needed to understand the interplay between sources and chemistry determining FT NO_2 distributions, but we see that the diurnal variation observed by TEMPO provides unique information.

In summary, we have presented a cloud-sliced FT NO_2 product from the TEMPO geostationary satellite instrument with high quality, high resolution, and the first diurnal coverage over North America. Combined with independent lightning observations from GLM, our data show evidence that lightning is the main source of FT NO_2 over North America outside winter and reveal large errors in a lightning NO_x emission scheme commonly used in atmospheric chemistry models. Further work is needed to disentangle the different processes contributing to model biases in FT NO_2, starting with improvement of the lightning parameterization to match the GLM spatial, seasonal, and diurnal patterns while remaining consistent with the model deep convection. Matching the observed diurnal variation of FT NO_2 will further evaluate NO_x chemistry. Overall, our data provide a unique resource to improve our understanding of FT NO_x and have implications for global tropospheric ozone and OH.

Materials and Methods

TEMPO Satellite Observations. TEMPO is a geostationary satellite instrument designed for monitoring of air quality over North America. It is on board the IntelSat-40e satellite launched in April 2023 and stationed at 91°W. It provides hourly daytime measurements over North America from 17°N to 60°N with a pixel resolution of 2.0 × 4.75 km^2 at 33.5°N. TEMPO measures solar backscatter in the ultraviolet-visible wavelength range (293 to 494 nm and 538 to 741 nm), enabling the retrieval of a suite of trace gases, aerosols, and cloud parameters (21). Here, we use the TEMPO L2 V03 cloud (40) and NO_2 (41) products from October 2023 (the beginning of nominal operations) to September 2024.

Cloud parameters are retrieved by TEMPO to support trace gas retrievals (42). We use two parameters: cloud radiance fraction (CRF), derived at 466 nm, and cloud optical centroid pressure (OCP), retrieved from the O_2–O_2 column near 477

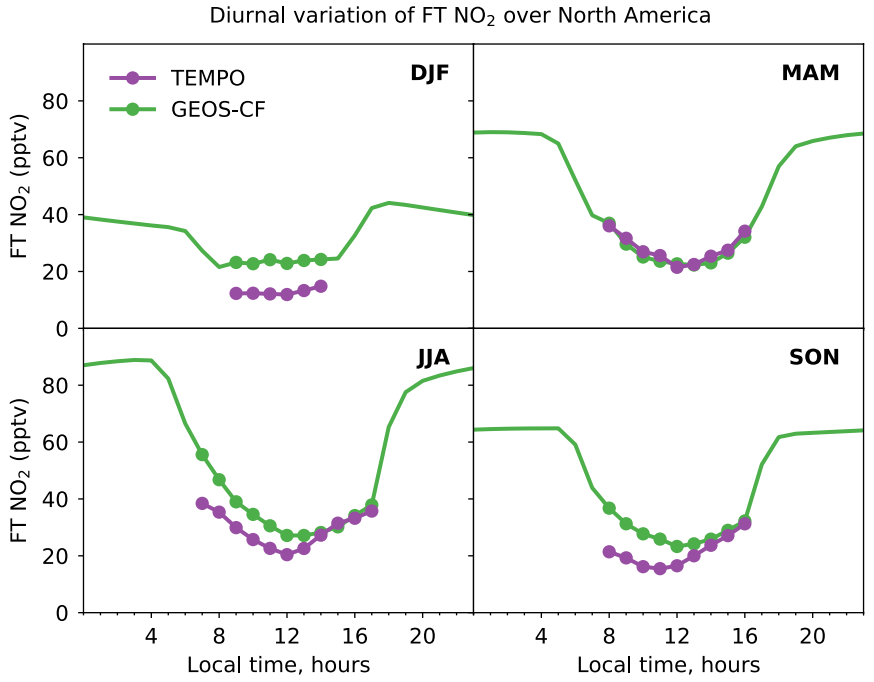

Fig. 4. Diurnal variation of FT (700 to 300 hPa) NO_2 mixing ratios averaged over the TEMPO domain for different seasons. TEMPO cloud-sliced observations are available for the hours indicated by symbols (9 to 14 LT for winter; 8 to 16 LT for spring and fall; 7 to 17 LT for summer) and are compared with GEOS-CF simulations sampled at the same locations and times. Outside of the TEMPO observing window, GEOS-CF results are shown as seasonal averages under all-sky conditions. The averages over the TEMPO domain are computed from the mean mixing ratios in 2° × 2.5° grid cells, and only grid cells with at least 10 seasonal observations for each hour are considered in the analysis.

nm. CRF is the fraction of observed radiance reflected by the cloud. OCP represents the pressure level where a proxy single-layer reflective cloud (with an albedo of 0.8) would be placed to quantify photon path length (43, 44). We define fully cloudy scenes as those with CRF > 0.9.

TEMPO NO_2 slant column densities (SCDs) along the optical path are retrieved by spectral fitting of backscattered solar radiances in the 405 to 465 nm window (45). For fully cloudy scenes, the observed SCDs are for the column above the OCP. We then derive the above-cloud NO_2 vertical column densities (VCDs) by dividing the SCDs by the air mass factor AMF_{cloudy} (18, 24), calculated as

$$AMF_{cloudy} = \int_{OCP}^{TOA} w(p)S(p)dp, \qquad [1]$$

where $w(p)$ is the pressure-dependent scattering weight obtained from a precomputed lookup table characterizing the instrument sensitivity to NO_2 at different altitudes, and $S(p)$ represents the relative vertical profile of NO_2 (shape factor) provided by the GEOS-CF model. Both $w(p)$ and $S(p)$ are provided in the TEMPO L2 NO_2 files. The integration is performed from the OCP to the top of atmosphere (TOA). For our analysis, we use above-cloud NO_2 VCDs for fully cloudy scenes (CRF > 0.9) with OCP between 700 and 300 hPa. Following standard practice (7, 46), we exclude data with quality flags > 0, solar zenith angle > 70°, surface albedo > 0.3, or snow/ice fraction > 0.

TEMPO Cloud-Slicing. The cloud-slicing technique infers the FT NO_2 mixing ratio from the slope of the regression line for above-cloud NO_2 VCDs versus cloud OCPs in adjacent fully cloudy scenes, assuming horizontal homogeneity in the NO_2 vertical profiles (17, 18). The use of linear regression to infer a FT mixing ratio assumes vertical homogeneity of NO_2 within the cloud-sliced layer. This assumption is generally reasonable for the 700 to 300 hPa free troposphere, where NO_2 vertical gradients are observed to be small (6, 47), but can be violated in the presence of strong NO_x plumes.

We perform the regressions for each TEMPO scan over 0.5° × 0.625° domains (50 × 50 km^2), selecting only those that contain at least 30 fully cloudy pixels, an OCP range exceeding 200 hPa and with sufficient variability (SD > 67 hPa), and a uniform NO_2 stratospheric column (relative SD < 0.02). We apply a Theil regression to minimize the influence of outliers (11). The regression slope is converted to NO_2 mixing ratio as described by Choi et al. (17). The SD of the slope (σ) is obtained with bootstrap resampling (n = 1,000). In each bootstrap iteration, cloud pressure-NO_2 column pairs are sampled with replacement to compute a slope. The SD across the 1,000 slope estimates defines σ. Slopes that are negative beyond two SD are removed (<5% of total estimates). From inspection of the data, we attribute these significantly negative slopes to NO_2 inhomogeneity within the 50 × 50 km^2 domain, where NO_2 lightning plumes from high-altitude clouds enhance NO_2 columns over these pixels but not over adjacent lower-altitude cloud scenes.

The FT NO_2 mixing ratios from individual 0.5° × 0.625° scenes are averaged to a 2° × 2.5° grid using weights proportional to $1/\sigma$, and the resulting 2° × 2.5° scenes are further averaged seasonally. Each 2° × 2.5° grid cell requires at least 20 FT NO_2 estimates from at least 10 different days to compute a seasonal average. When deriving the FT NO_2 diurnal product (Fig. 4), we relax the criteria to 10 estimates per season for a given hour of day.

Errors in our FT NO_2 product arise from the cloud retrievals, the NO_2 column retrievals, and the regression which assumes a uniform NO_2 mixing ratio within the 700 to 300 hPa layer over a 50 × 50 km^2 domain. The CRF retrieved by TEMPO may have a high bias of ~0.05 (42), but we find that a stricter threshold for fully cloudy scenes (CRF > 0.95) does not change results significantly. Sensitivity studies show that OCP uncertainties are on the order of a few tens of hPa with respect to a variety of parameters for CRF >0.9 (42), although detailed validation has not been reported against other cloud products. The below-cloud NO_2 contribution is typically <1% of total SCDs for CRF >0.9 and has little impact on the results when subtracted upfront. The sensitivity of AMF_{cloudy} to the vertical NO_2 shape factor is less than 5% (24) due to the nearly uniform scattering weights above clouds. We found that using a geometric AMF instead of AMF_{cloudy} introduces a low bias of ~2 pptv (10%) for seasonal FT NO_2. The NO_2 SCDs retrievals have a precision about 5 × 10^{14} molec cm^{-2} after normalization by geometric AMF (45). NO_2 retrievals in the early morning and late afternoon may be biased (45) but this would have little impact on the cloud-sliced results as the biases would cancel out in the regression. The SD on the regression slope for NO_2 VCD versus cloud OCP determined from bootstrap resampling has a median value of 60% for individual estimates, but that error would decrease with averaging.

To estimate an overall error statistic for our seasonal FT NO_2 product on the 2° × 2.5° grid, we use the normalized mean bias (NMB) and SD of the differences between TEMPO and aircraft observations (Fig. 2*A*). From there, we infer an accuracy of 13% and precision of 50%. This is conservative because it assumes that the aircraft data are accurate and representative of the TEMPO observations. A significant fraction of the difference could instead originate from representation error considering that the aircraft campaigns were conducted with only limited sampling of vertical profiles and for different years.

Aircraft Observations. We use aircraft observations from the INTEX-B, ARCTAS, DC-3, SEAC^{4}RS, DISCOVER-AQ, FRAPPE, WINTER, and AEROMMA campaigns over North America to evaluate our cloud-sliced FT NO_2 product. These campaigns operated a DC-8 (up to 12 km), GV (up to 12 km), or C-130 (up to 7 km) aircraft (*SI Appendix*, Table S1*A*). To compare with our cloud-sliced product, we focus on flight segments between 3 to 9 km altitude (~700 to 300 hPa) with a minimum vertical profiling of 3 km altitude within each 2° × 2.5° grid cell. The two winter campaigns, DISCOVER-AQ (California flights) and WINTER, have limited vertical extent (with ceilings of 3.2 to 5 km), and for those, we include all data above 3 km without applying the vertical extent filter.

SI Appendix, Table S1*B* lists the measurements used in this work. NO_2 measurements in the free troposphere can be affected by positive interference from the thermal decomposition of labile NO_x reservoirs due to higher instrument temperatures compared to ambient air (48–51). To avoid these artifacts and following approaches from previous studies (6, 11, 52), we calculate PSS NO_2 from NO measurements by assuming a dynamic daytime equilibrium between fast oxidation of NO and photolysis of NO_2. NO oxidation in the FT is mainly driven by O_3, with a smaller contribution from HO_2 (14, 52). PSS NO_2 is then calculated as

$$[NO_2]_{PSS} = [NO] \times \frac{k_1[O_3] + k_2[HO_2]}{j_{NO_2}}, \quad [2]$$

where k represents rate constants (53), [] denotes number density, and j_{NO2} is the NO_2 photolysis frequency. PSS NO_2 is computed from aircraft measurements, except for $[HO_2]$ in campaigns where it was not measured (*SI Appendix*, Table S1*B*). In these cases, $k_2[HO_2]$ is estimated based on its relative contribution to $(k_1[O_3] + k_2[HO_2])$ using data from other campaigns where $[HO_2]$ measurements are available. For the AEROMMA campaign, we use directly measured NO_2 from a newly developed laser-induced fluorescence instrument (54), in which the NO_2 photolytic converter is maintained at near-ambient temperatures to minimize interference.

We use only daytime aircraft observations (9 to 16 LT for winter and 8 to 17 LT for other seasons) for consistency with the TEMPO observing time window. Additional filtering is applied to exclude observations affected by fresh convection (number concentration of condensation nuclei larger than 10 nm > 5 × 10^3 cm^{-3}), fresh NO_x emissions (NO_y/NO < 3 mol mol^{-1}), and biomass burning plumes (CO > 200 ppbv and CH_3CN > 200 pptv; CO > 500 ppbv or CH_3CN > 500 pptv if one of these observations is unavailable). Flights focused on sampling deep convection or fire plumes are also excluded (*SI Appendix*, Table S1*A*) (55–57). We then average the FT NO_2 concentrations within each 2° × 2.5° grid cell for each flight and compute the seasonal mean for each grid cell across all flights.

GOES GLM Observations. We use satellite-based lightning flash observations from the two GLM instruments onboard GOES-16 and GOES-18, with GOES-16 covering the eastern Americas (centered at 75.2°W), GOES-18 covering the western Americas (centered at 137.2°W), and both providing latitudinal coverage from 54°S to 54°N. GLM is an optical imager that detects cloud top lightning illumination at 777.4 nm every 2 ms, with a nadir pixel resolution of 8 km (22). The GLM retrieval algorithm defines a lightning event as the occurrence of a single pixel exceeding the background radiance threshold. It further aggregates simultaneous adjacent events into groups and clusters sequential groups separated by less than 330 ms and 16.5 km into a single flash (58). The GLM Level 2 product reports the radiance-weighted centroids of lightning flash locations, which we map to the 0.5° × 0.625° grid. To minimize the degradation in data quality near the edge of each instrument's field of view, we use GLM data from GOES-16 for regions east of 106.2°W and from GOES-18 for regions west of 106.2°W (59).

Data, Materials, and Software Availability. The TEMPO cloud and NO_2 products are publicly available at https://asdc.larc.nasa.gov/project/TEMPO?level=2 (60). Aircraft observations for the INTEX-B, ARCTAS, DC-3, SEAC^{4}RS, DISCOVER-AQ, and FRAPPE campaigns are available at https://www-air.larc.nasa.gov/missions/merges/ (61). Data for the WINTER campaign are available at https://www.eol.ucar.edu/field_projects/winter (62), and data for the AEROMMA campaign are available at https://csl.noaa.gov/projects/aeromma/data.html (63). GLM lightning flash L2 data are available at https://noaa-goes16.s3.amazonaws.com/index.html#GLM-L2-LCFA/ (64). GEOS-CF simulated NO_2 vertical profiles are included with the TEMPO NO_2 product. Emission input data for GEOS-CF are publicly available at https://portal.nccs.nasa.gov/datashare/gmao/geos-cf/v1/ (65). TROPOMI FT NO_2 is on the UCL Data Repository (https://doi.org/10.5522/04/28846736) (66). TEMPO FT NO_2 seasonal product is archived at Zenodo (https://zenodo.org/records/15299339) (67).

ACKNOWLEDGMENTS. We are grateful to the instrument teams of the INTEX-B, ARCTAS, DC-3, SEAC^{4}RS, DISCOVER-AQ, FRAPPE, WINTER, and AEROMMA campaigns for making their data freely available. This work was supported by the Harvard-NUIST Joint Laboratory for Air Quality and Climate. TEMPO operations and data processing at the Smithsonian Astrophysical Observatory are supported by NASA contracts NNL13AA09C and 80MSFC24CA004. E.A.M. acknowledges the support from the European Research Council under the European Union's Horizon 2020 research and innovation programme (through a Starting Grant awarded to E.A.M, UpTrop [grant no. 851854]).

Author affiliations: [a]John A. Paulson School of Engineering and Applied Sciences, Harvard University, Cambridge, MA 02138; [b]Atomic and Molecular Physics Division, Center for Astrophysics | Harvard and Smithsonian, Cambridge, MA 02138; [c]Global Modeling and Assimilation Office, NASA Goddard Space Flight Center, Greenbelt, MD 20771; [d]GESTAR II, Morgan State University, Baltimore, MD 21251; [e]Department of Geography, University College London, London WC1E 6BT, United Kingdom; [f]NOAA Chemical Sciences Laboratory, Boulder, CO 80305; [g]NASA Langley Research Center, Hampton, VA 23666; and [h]Jiangsu Key Laboratory of Atmospheric Environment Monitoring and Pollution Control, Collaborative Innovation Center of Atmospheric Environment and Equipment Technology, School of Environmental Science and Engineering, Nanjing University of Information Science and Technology, Nanjing 210044, China

Author contributions: R.D. and D.J.J. designed research; R.D. performed research; R.D., H.W., C.R.N., G.G.A., H.C., X.L., V.S., L.H.Y., Y.J.O., E.A.M., R.P.H., A.W.R., J.H.C., K.L., and H.L. analyzed data; H.W., C.R.N., G.G.A., H.C., and X.L. provided guidance on the TEMPO satellite data; E.A.M. and R.P.H. supplied the reprocessed TROPOMI cloud-sliced NO_2 product; A.W.R. and J.H.C. provided guidance on aircraft observations; and R.D. and D.J.J. wrote the paper.

1. J. Lelieveld, S. Gromov, A. Pozzer, D. Taraborrelli, Global tropospheric hydroxyl distribution, budget and reactivity. *Atmos. Chem. Phys.* **16**, 12477–12493 (2016).
2. L. T. Murray, A. M. Fiore, D. T. Shindell, V. Naik, L. W. Horowitz, Large uncertainties in global hydroxyl projections tied to fate of reactive nitrogen and carbon. *Proc. Natl. Acad. Sci. U.S.A.* **118**, e2115204118 (2021).
3. A. M. Fiore, L. J. Mickley, Q. Zhu, C. B. Baublitz, Climate and tropospheric oxidizing capacity. *Annu. Rev. Earth Planet. Sci.* **52**, 321–349 (2024).
4. C. M. Nussbaumer *et al.*, Ozone formation sensitivity to precursors and lightning in the tropical troposphere based on airborne observations. *J. Geophys. Res. Atmos.* **129**, e2024JD041168 (2024).
5. L. Jaeglé *et al.*, Sources and chemistry of NOx in the upper troposphere over the United States. *Geophys. Res. Lett.* **25**, 1705–1708 (1998).
6. V. Shah *et al.*, Nitrogen oxides in the free troposphere: Implications for tropospheric oxidants and the interpretation of satellite NO2 measurements. *Atmos. Chem. Phys.* **23**, 1227–1257 (2023).
7. R. Dang *et al.*, Background nitrogen dioxide (NO2) over the United States and its implications for satellite observations and trends: Effects of nitrate photolysis, aircraft, and open fires. *Atmos. Chem. Phys.* **23**, 6271–6284 (2023).
8. L. T. Murray, D. J. Jacob, J. A. Logan, R. C. Hudman, W. J. Koshak, Optimized regional and interannual variability of lightning in a global chemical transport model constrained by LIS/OTD satellite data. *J. Geophys. Res. Atmos.* **117**, D20307 (2012).
9. D. J. Allen *et al.*, Observations of lightning NOx production from GOES-R post launch test field campaign flights. *J. Geophys. Res. Atmos.* **126**, e2020JD033769 (2021).
10. K. A. Cummings *et al.*, Evaluation of lightning flash rate parameterizations in a cloud-resolved WRF-Chem simulation of the 29–30 May 2012 Oklahoma severe supercell system observed during DC3. *J. Geophys. Res. Atmos.* **129**, e2023JD039492 (2024).
11. R. P. Horner, E. A. Marais, N. Wei, R. G. Ryan, V. Shah, Vertical profiles of global tropospheric nitrogen dioxide (NO2) obtained by cloud slicing the TROPOspheric Monitoring Instrument (TROPOMI). *Atmos. Chem. Phys.* **24**, 13047–13064 (2024).
12. J. Mao *et al.*, Global impact of lightning-produced oxidants. *Geophys. Res. Lett.* **48**, e2021GL095740 (2021).
13. B. A. Nault *et al.*, Lightning no emissions: Reconciling measured and modeled estimates with updated NO chemistry. *Geophys. Res. Lett.* **44**, 9479–9488 (2017).

14. R. F. Silvern *et al.*, Observed NO/NO2 ratios in the upper troposphere imply errors in NO-NO2-O3 cycling kinetics or an unaccounted NOx reservoir. *Geophys. Res. Lett.* **45**, 4466–4474 (2018).
15. B. A. Nault *et al.*, Observational constraints on the oxidation of NOx in the upper troposphere. *J. Phys. Chem. A.* **120**, 1468–1478 (2016).
16. V. Shah *et al.*, Particulate nitrate photolysis as a possible driver of rising tropospheric ozone. *Geophys. Res. Lett.* **51**, e2023GL107980 (2024).
17. S. Choi *et al.*, First estimates of global free-tropospheric NO2 abundances derived using a cloud-slicing technique applied to satellite observations from the Aura Ozone Monitoring Instrument (OMI). *Atmos. Chem. Phys.* **14**, 10565–10588 (2014).
18. M. Belmonte Rivas, P. Veefkind, H. Eskes, P. Levelt, OMI tropospheric NO2 profiles from cloud slicing: Constraints on surface emissions, convective transport and lightning NOx. *Atmos. Chem. Phys.* **15**, 13519–13553 (2015).
19. E. A. Marais *et al.*, Nitrogen oxides in the global upper troposphere: Interpreting cloud-sliced NO2 observations from the OMI satellite instrument. *Atmos. Chem. Phys.* **18**, 17017–17027 (2018).
20. E. A. Marais *et al.*, New observations of NO2 in the upper troposphere from TROPOMI. *Atmos. Meas. Tech.* **14**, 2389–2408 (2021).
21. P. Zoogman *et al.*, Tropospheric emissions: Monitoring of pollution (TEMPO). *J. Quant. Spectrosc. Radiat. Transf.* **186**, 17–39 (2017).
22. S. D. Rudlosky, S. J. Goodman, K. S. Virts, E. C. Bruning, Initial geostationary lightning mapper observations. *Geophys. Res. Lett.* **46**, 1097–1104 (2019).
23. T. H. Bertram *et al.*, Direct measurements of the convective recycling of the upper troposphere. *Science* **315**, 816–820 (2007).
24. J. L. Laughner, R. C. Cohen, Quantification of the effect of modeled lightning NO2 on UV–visible air mass factors. *Atmos. Meas. Tech.* **10**, 4403–4419 (2017).
25. R. F. Silvern *et al.*, Using satellite observations of tropospheric NO2 columns to infer long-term trends in US NOx emissions: The importance of accounting for the free tropospheric NO2 background. *Atmos. Chem. Phys.* **19**, 8863–8878 (2019).
26. K. Miyazaki, H. J. Eskes, K. Sudo, Global NOx emission estimates derived from an assimilation of OMI tropospheric NO2 columns. *Atmos. Chem. Phys.* **12**, 2263–2288 (2012).
27. V. Shah *et al.*, Effect of changing NOx lifetime on the seasonality and long-term trends of satellite-observed tropospheric NO2 columns over China. *Atmos. Chem. Phys.* **20**, 1483–1495 (2020).
28. J. F. Lamarque, G. P. Brasseur, P. G. Hess, J. F. Müller, Three-dimensional study of the relative contributions of the different nitrogen sources in the troposphere. *J. Geophys. Res. Atmos.* **101**, 22955–22968 (1996).
29. H. Levy Ii, W. J. Moxim, A. A. Klonecki, P. S. Kasibhatla, Simulated tropospheric NO: Its evaluation, global distribution and individual source contributions. *J. Geophys. Res. Atmos.* **104**, 26279–26306 (1999).
30. C. A. Keller *et al.*, Description of the NASA GEOS composition forecast modeling system GEOS-CF v1.0. *J. Adv. Model. Earth Syst.* **13**, e2020MS002413 (2021).
31. G. Janssens-Maenhout *et al.*, HTAP_v2.2: A mosaic of regional and global emission grid maps for 2008 and 2010 to study hemispheric transport of air pollution. *Atmos. Chem. Phys.* **15**, 11411–11432 (2015).
32. EPA, Air pollutant emissions trends data. https://www.epa.gov/air-emissions-inventories/air-pollutant-emissions-trends-data. Accessed 10 March 2025.
33. M. Val Martin *et al.*, Smoke injection heights from fires in North America: Analysis of 5 years of satellite observations. *Atmos. Chem. Phys.* **10**, 1491–1510 (2010).
34. M. Val Martin, R. A. Kahn, M. G. Tosca, A global analysis of wildfire smoke injection heights derived from space-based multi-angle imaging. *Remote Sens.* **10**, 1609 (2018).
35. J. F. J. Calahorrano *et al.*, Daytime oxidized reactive nitrogen partitioning in western US wildfire smoke plumes. *J. Geophys. Res. Atmos.* **126**, e2020JD033484 (2021).
36. C. Price, D. Rind, A simple lightning parameterization for calculating global lightning distributions. *J. Geophys. Res. Atmos.* **97**, 9919–9933 (1992).
37. R. C. Hudman *et al.*, Surface and lightning sources of nitrogen oxides over the United States: Magnitudes, chemical evolution, and outflow. *J. Geophys. Res. Atmos.* **112**, D12S05 (2007).
38. L. H. Yang *et al.*, Interpreting geostationary environment monitoring spectrometer (GEMS) geostationary satellite observations of the diurnal variation in nitrogen dioxide (NO2) over East Asia. *Atmos. Chem. Phys.* **24**, 7027–7039 (2024).
39. D. P. Edwards *et al.*, Quantifying the diurnal variation in atmospheric NO2 from Geostationary Environment Monitoring Spectrometer (GEMS) observations. *Atmos. Chem. Phys.* **24**, 8943–8961 (2024).
40. NASA/LARC/SD/ASDC, TEMPO cloud pressure and fraction (O2-O2 dimer) V03 (PROVISIONAL). https://doi.org/10.5067/IS-40e/TEMPO/CLDO4_L2.003. Accessed 29 September 2025.
41. NASA/LARC/SD/ASDC, TEMPO NO2 tropospheric and stratospheric columns V03 (PROVISIONAL). https://doi.org/10.5067/IS-40e/TEMPO/NO2_L2.003. Accessed 29 September 2025.
42. H. Wang *et al.*, Algorithm theoretical basis for version 3 TEMPO O2–O2 cloud product. *Earth Space Sci.* **12**, e2024EA004165 (2025).
43. J. Joiner *et al.*, Fast simulators for satellite cloud optical centroid pressure retrievals; Evaluation of OMI cloud retrievals. *Atmos. Meas. Tech.* **5**, 529–545 (2012).
44. A. Vasilkov *et al.*, A cloud algorithm based on the O2–O2 477 nm absorption band featuring an advanced spectral fitting method and the use of surface geometry-dependent Lambertian-equivalent reflectivity. *Atmos. Meas. Tech.* **11**, 4093–4107 (2018).
45. C. Nowlan, G. González Abad, X. Liu, H. Wang, K. Chance, "TEMPO Nitrogen Dioxide Retrieval Algorithm Theoretical Basis Document" (Version 1.0, Center for Astrophysics | Harvard and Smithsonian, Cambridge, MA, 2025). 10.5067/WX026254FI2U.
46. Z. Qu *et al.*, US COVID-19 shutdown demonstrates importance of background NO2 in inferring NOx emissions from satellite NO2 observations. *Geophys. Res. Lett.* **48**, e2021GL092783 (2021).
47. K. R. Travis *et al.*, Why do models overestimate surface ozone in the Southeast United States? *Atmos. Chem. Phys.* **16**, 13561–13577 (2016).
48. E. C. Browne *et al.*, Global and regional effects of the photochemistry of CH3O2NO2: Evidence from ARCTAS. *Atmos. Chem. Phys.* **11**, 4209–4219 (2011).
49. B. A. Nault *et al.*, Measurements of CH3O2NO2 in the upper troposphere. *Atmos. Meas. Tech.* **8**, 987–997 (2015).
50. C. Reed, M. J. Evans, P. Di Carlo, J. D. Lee, L. J. Carpenter, Interferences in photolytic NO2 measurements: Explanation for an apparent missing oxidant? *Atmos. Chem. Phys.* **16**, 4707–4724 (2016).
51. C. M. Nussbaumer *et al.*, Modification of a conventional photolytic converter for improving aircraft measurements of NO2 via chemiluminescence. *Atmos. Meas. Tech.* **14**, 6759–6776 (2021).
52. L. H. Yang *et al.*, Tropospheric NO2 vertical profiles over South Korea and their relation to oxidant chemistry: Implications for geostationary satellite retrievals and the observation of NO2 diurnal variation from space. *Atmos. Chem. Phys.* **23**, 2465–2481 (2023).
53. J. B. Burkholder *et al.*, Chemical kinetics and photochemical data for use in atmospheric studies; evaluation number 19. JPL Open Repository. https://hdl.handle.net/2014/49199. Deposited 1 May 2020.
54. A. W. Rollins *et al.*, Single-photon laser-induced fluorescence detection of nitric oxide at sub-parts-per-trillion mixing ratios. *Atmos. Meas. Tech.* **13**, 2425–2439 (2020).
55. M. C. Barth *et al.*, The deep convective clouds and chemistry (DC3) field campaign. *Bull. Amer. Meteorol. Soc.* **96**, 1281–1309 (2015).
56. O. B. Toon *et al.*, Planning, implementation, and scientific goals of the Studies of Emissions and Atmospheric Composition, Clouds and Climate Coupling by Regional Surveys (SEAC4RS) field mission. *J. Geophys. Res. Atmos.* **121**, 4967–5009 (2016).
57. X. Liu *et al.*, Agricultural fires in the southeastern U.S. during SEAC4RS: Emissions of trace gases and particles and evolution of ozone, reactive nitrogen, and organic aerosol. *J. Geophys. Res. Atmos.* **121**, 7383–7414 (2016).
58. S. J. Goodman *et al.*, The GOES-R geostationary lightning mapper (GLM). *Atmos. Res.* **125–126**, 34–49 (2013).
59. Y. Wu, A. Pour-Biazar, W. J. Koshak, P. Cheng, LNOx emission model for air quality and climate studies using satellite lightning mapper observations. *J. Geophys. Res. Atmos.* **128**, e2022JD037406 (2023).
60. NASA/LARC/SD/ASDC, TEMPO Level 2 V03 products. NASA EARTHDATA ASDC. https://asdc.larc.nasa.gov/project/TEMPO?level=2. Accessed 29 September 2025.
61. NASA field campaign science teams, NASA Tropospheric Chemistry Campaigns Data. NASA LaRC Suborbital Science Data for Atmospheric Composition. https://www-air.larc.nasa.gov/missions/merges/. Accessed 29 September 2025.
62. WINTER science team, WINTER field campaign data. UCAR EOL Data Archive. https://www.eol.ucar.edu/field_projects/winter. Accessed 29 September 2025.
63. AEROMMA science team, AEROMMA field campaign data. NOAA CSL Data Repository. https://csl.noaa.gov/projects/aeromma/data.html. Accessed 29 September 2025.
64. NOAA, GLM lightning flash Level 2 data. AWS. https://noaa-goes16.s3.amazonaws.com/index.html#GLM-L2-LCFA/. Accessed 29 September 2025.
65. NASA GMAO, GEOS-CF v1 simulation diagnostics. NASA Center for Climate Simulation. https://portal.nccs.nasa.gov/datashare/gmao/geos-cf/v1/. Accessed 29 September 2025.
66. R. P. Horner, E. A. Marais, Free tropospheric nitrogen dioxide concentrations from cloud-slicing TROPOMI. UCL Data Repository. https://doi.org/10.5522/04/28846736. Deposited 1 August 2025.
67. R. Dang *et al.*, Free tropospheric nitrogen dioxide concentrations from cloud-slicing TEMPO. Zenodo. https://zenodo.org/records/15299339. Deposited 28 April 2025.